

GMC COLLISIONS AS TRIGGERS OF STAR FORMATION. V. OBSERVATIONAL SIGNATURES

THOMAS G. BISBAS^{1,2}, KEI E. I. TANAKA¹, JONATHAN C. TAN^{1,3,4}, BENJAMIN WU⁴, AND FUMITAKA NAKAMURA⁴

Draft version November 10, 2018

ABSTRACT

We present calculations of molecular, atomic and ionic line emission from simulations of giant molecular cloud (GMC) collisions. We post-process snapshots of the magneto-hydrodynamical simulations presented in an earlier paper in this series by Wu et al. (2017a) of colliding and non-colliding GMCs. Using photodissociation region (PDR) chemistry and radiative transfer we calculate the level populations and emission properties of $^{12}\text{CO } J = 1 - 0$, $[\text{C I}] \ ^3\text{P}_1 \rightarrow \ ^3\text{P}_0$ at $609 \mu\text{m}$, $[\text{C II}] \ 158 \mu\text{m}$ and $[\text{O I}] \ ^3\text{P}_1 \rightarrow \ ^3\text{P}_0$ transition at $63 \mu\text{m}$. From integrated intensity emission maps and position-velocity diagrams, we find that fine-structure lines, particularly the $[\text{C II}] \ 158 \mu\text{m}$, can be used as a diagnostic tracer for cloud-cloud collision activity. These results hold even in more evolved systems in which the collision signature in molecular lines has been diminished.

Keywords: ISM: clouds — ISM: kinematics and dynamics — ISM: lines and bands — ISM: magnetic fields — ISM: structure — methods: numerical

1. INTRODUCTION

Giant Molecular Cloud (GMC) collisions are a potential mechanism for triggering star formation activity in such clouds (e.g. Scoville et al. 1986; Tan 2000; Higuchi et al. 2010; Duarte-Cabral et al. 2010; Fukui et al. 2014; Balfour et al. 2015; Torii et al. 2017a). Models of galactic shear-driven collisions (Gammie et al. 1991; Tan 2000; Tasker & Tan 2009; Dobbs et al. 2015) may help explain global galactic star formation relations (Tan 2010; Suwannajak et al. 2014). GMC collisions may also be an important mechanism for driving turbulence within GMCs (Tan et al. 2013; Jin et al. 2017; Li et al. 2017). Thus it is important to develop theoretical and numerical models for such collisions and then use them to calculate the observational signatures of these events (e.g., Duarte-Cabral et al. 2011; Inoue & Fukui 2013; Takahira et al. 2014; Haworth et al. 2015a,b).

With the above goal in mind, this paper continues the works of Wu et al. (2015, 2017a) (Papers I and II) in studying GMC collisions via ideal magneto-hydrodynamic (MHD) simulations. In particular, Paper II studied the kinematics and dynamics of collisions of turbulent, magnetized, multiphase (via photodissociation region (PDR)-based heating/cooling functions) GMCs using synthetic observations in the optically thin limit. Here, we provide a more realistic treatment of the radiative transfer of line emission from multiple species from these simulations with a tool we develop that accounts for velocity-dependent optical depth along the line-of-sight. Other papers in this series have added additional physics: Wu et al. (2017b) (Paper III) incorporated star formation via various sub-grid models, including simulations in which star formation depends on the local mass to magnetic flux ratio; Christie et al. (2017) (Paper IV) studied the effects of ambipolar diffusion, especially its effects on the efficiency of dense core formation. However, here, with our focus on observational signa-

tures, especially on the larger, global scales of the GMCs, we return to the simulation outputs of Paper II for our analysis. We note that these simulations do not include star formation or any localized feedback, so the results we present will isolate the “pure” signature of the GMC-GMC collision process, separate from these complicating factors.

Our paper is organized as follows. In §2 we give a brief outline of the snapshots we selected of the MHD simulations performed in Paper II (§2.1), of the PDR calculations (§2.2) and of the radiative transfer tool we develop (§2.3). In §3 we discuss the signatures frequently used by the observational community to identify cloud-cloud collision activity. In §4 we report our results, which are then further discussed in §5. We conclude in §6.

2. NUMERICAL METHODS

2.1. Magneto-hydrodynamical simulations

For the purposes of this work we use two snapshots from the three-dimensional MHD simulations performed in Paper II. These simulations include self-gravity, supersonic turbulence and magnetic fields (treated in the limit of ideal MHD). They have been performed with the adaptive-mesh refinement (AMR) code ENZO (Bryan et al. 2014).

The two GMCs considered are initially spherical and uniform with total H-nucleus number density of $n_{\text{H}} = 100 \text{ cm}^{-3}$, radius of $R = 20 \text{ pc}$ and thus with mass of $M = 9.3 \times 10^4 M_{\odot}$. As described in Paper II, for simplicity the mean particle mass was set to a constant value of $\mu = 2.33 m_{\text{H}}$, where m_{H} is the mass of the Hydrogen atom. In addition, a constant adiabatic index of $\gamma = 5/3$ was adopted as the most appropriate single valued choice for a focus on the dynamics of the molecular clouds. The ambient medium around the GMCs consists of gas with $n_{\text{H}} = 10 \text{ cm}^{-3}$. The spatial resolution of the AMR grid has a minimum value of 0.125 pc . A magnetic field with strength $B = 10 \mu\text{G}$ has been included, directed at an angle of $\theta = 60^\circ$ with respect to x -direction. The centers of GMCs have an initial separation of $2R$ in the x -direction and 0 in the z -direction. Along the y -direction they are offset by an impact parameter $b = 0.5R$. Both GMCs have a one-dimensional turbulent velocity dispersion of $\sigma_v = 5.2 \text{ km s}^{-1}$.

As described in Paper I, the simulations include PDR-based

Electronic address: TGB: tbsbas@ufl.edu

¹ Department of Astronomy, University of Florida, Gainesville, FL 32611, USA

² Max-Planck-Institut für Extraterrestrische Physik, Giessenbachstrasse 1, D-85748 Garching, Germany

³ Department of Physics, University of Florida, Gainesville, FL 32611, USA

⁴ National Astronomical Observatory of Japan, Mitaka, Tokyo, 181-8588, Japan

heating and cooling processes to determine gas and dust temperature and the emission properties from various species. We note that these heating and cooling functions are applied to both the GMCs and the ambient medium, so that the thermal and chemical evolution of the gas across the atomic to molecular transition is well-modeled. An isotropic FUV radiation field with strength $G/G_0 = 4$ (i.e., 4 times the Habing 1968, estimate of the local FUV intensity) and a cosmic-ray ionization rate of $\zeta_{\text{CR}} = 10^{-16} \text{ s}^{-1}$ have been adopted. These values represent conditions observed in the inner part of the Galaxy at distances of $\sim 4 \text{ kpc}$ from the Galactic Centre. Further details are discussed in Papers I and II.

We select two different cases from the above set of simulations: i) the case where the clouds collide at a relative speed of $v_{\text{rel}} = 10 \text{ km s}^{-1}$ (“colliding”) in which they are moving at equal but opposite velocities along the axis of collision (i.e., $+v_{\text{rel}}/2 = +5 \text{ km s}^{-1}$ and $-v_{\text{rel}}/2 = -5 \text{ km s}^{-1}$), and ii) the case where the clouds do not collide (“non-colliding”) but overlap each other along the line-of-sight, therefore the relative speed is $v_{\text{rel}} = 0 \text{ km s}^{-1}$. The selected snapshots for the colliding case are at times of $t = 2$ and 4 Myr and are shown in the top and middle rows of Fig. 1. The collision occurs along the x -direction. For the non-colliding case, we consider only the snapshot at $t = 4 \text{ Myr}$, which is shown at the bottom row of Fig. 1.

2.2. 3D-PDR calculations

To perform realistic radiative transfer calculations (see §2.3) and obtain the emission map of a particular line, we need knowledge of the corresponding level populations, abundances of species, as well as gas and dust temperature profiles. To do this, we use the 3D-PDR code⁵ (Bisbas et al. 2012), which treats the chemistry of PDRs using various cooling and heating processes. Although the code is able to calculate three-dimensional PDRs of arbitrary density distributions, the computational cost for post-processing the above hydrodynamical snapshots at the given resolution is prohibitively high. Instead, we perform an extended one-dimensional grid of uniform density slabs irradiated by a plane-parallel radiation field and we adopt the methodology described in Paper I, which connects the H-nucleus number density n_{H} of a cell with a most probable visual extinction value, A_V .

The density range spanning the grid of one-dimensional simulations is $1 \text{ cm}^{-3} < n_{\text{H}} < 10^7 \text{ cm}^{-3}$, with a sampling every 0.1 dex. This resolution gives a total set of 70 simulations. In all these calculations we considered a plane-parallel radiation field with strength $\chi/\chi_0 = 4$ and a cosmic-ray ionization rate of $\zeta_{\text{CR}} = 10^{-16} \text{ s}^{-1}$, thus mimicking the conditions adopted in Papers I and II. We utilized a reduced UMIST 2012 chemical network (McElroy et al. 2013) of 33 species and 330 reactions and we adopted the “standard” ISM abundances of elements, i.e., $[\text{He}]/[\text{H}] = 0.1$, $[\text{C}]/[\text{H}] = 10^{-4}$, and $[\text{O}]/[\text{H}] = 3 \times 10^{-4}$ (Röllig et al. 2007; Cartledge et al. 2004; Cardelli et al. 1996).

There is generally good agreement between the grids of 1D simulations of Wu et al. (2015), which used the simpler Py-PDR code, and this work. However, in the low density medium that corresponds to low values of A_V we do find some differences in abundances and other properties, which is not unexpected since PDR codes often deviate in this regime (Röllig et al. 2007). This leads to moderate differences in the

calculated mass-weighted gas temperature of Fig. 1 in comparison with Wu et al. (2017a).

2.3. Radiative Transfer calculations

We construct a radiative transfer tool described in Appendix A which we use for our synthetic observations. As mentioned in §2.1, the MHD simulations use an AMR grid, effectively meaning that the spatial resolution is higher in places of higher density. For the radiative transfer calculations, however, we convert the selected snapshots to an uniform grid of 0.125 pc resolution. This in turn gives a grid consisting of 512^3 cells which we use to solve for the radiative transfer along each line-of-sight.

Once the radiative transfer equation is solved (see Appendix A), we calculate the antenna temperature⁶, T_A , using the following relation:

$$T_A = \frac{c^2 I_\nu}{2k_{\text{B}}\nu^2}. \quad (1)$$

Here, c is the speed of light, k_{B} is the Boltzmann constant, and I_ν is the intensity over frequency ν , defined as

$$\nu = \nu_0 \left(1 - \frac{v_{\text{los}}}{c} \right), \quad (2)$$

where ν_0 denotes the frequency in the observer reference frame and v_{los} is the velocity along the line-of-sight. The integrated antenna temperature over velocity, W , is evaluated as

$$W = \int T_A dv_{\text{los}}, \quad (3)$$

where the velocity width adopted to construct the emission maps is $-15 \text{ km s}^{-1} < v_{\text{los}} < +15 \text{ km s}^{-1}$.

Unless otherwise stated, the radiative transfer algorithm has been applied along the x -direction, which is the axis of collision. The chosen direction of integration is from $+x$ to $-x$, i.e., the observer is located in the $-x$ direction. With the collision occurring along the line-of-sight, we expect to see the clearest signature of its effects in velocity space in this limiting case. However, we will also examine how the GMCs appear when viewed from a direction perpendicular to the collision axis, which is the other extreme, i.e., for which the signatures of the collision would be minimized.

3. THE “BRIDGE-EFFECT” SIGNATURE

An observational technique to identify a collision event between two clouds is to construct their position-velocity (p-v) diagram and look for two velocity peaks along the line-of-sight. Each velocity peak corresponds to one individual cloud. In the p-v diagram, the peaks in T_A along the velocity axis at a particular position, should be connected via a “bridge” of lower T_A . This “bridge-effect” indicates the presence of a pair of clouds along the line-of-sight that are connected by gas at intermediate velocities between the two main values of each cloud, implying a mutual interaction. Otherwise (i.e., when the velocity peaks are not connected but remain isolated), one may simply be seeing two different clouds along the line-of-sight that are not interacting with one another.

Bridged velocity peaks have been observed in various cases. For example, $\text{C}^{18}\text{O } J = 1-0$ observations in the Serpens star-forming region by Duarte-Cabral et al. (2010) confirm the ex-

⁵ <https://uclchem.github.io/3dpdr.html>

⁶ Following the notation of Draine (2011)

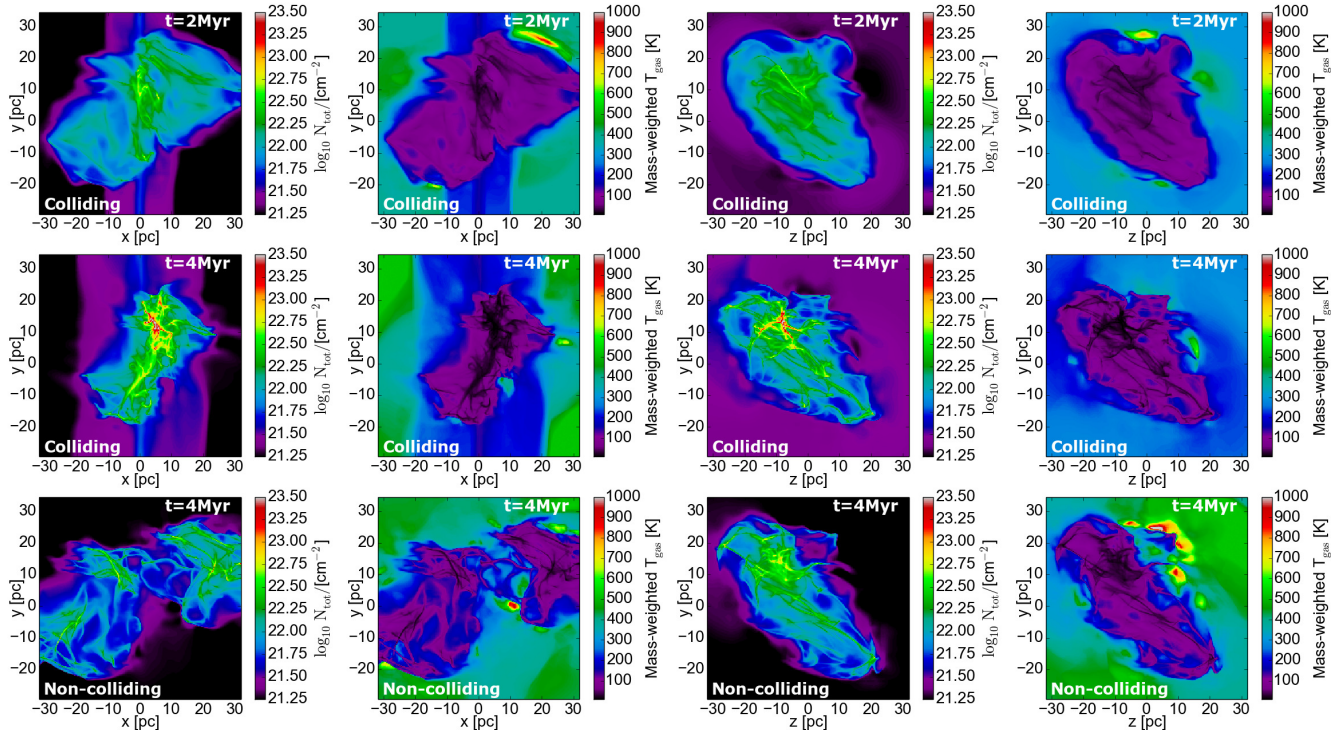


Figure 1. Maps of the total H-nucleus column density (first and third columns) and mass-weighted gas temperature (second and fourth columns) of the MHD simulations from Paper II. The integration in the maps of the first two columns is along the z -direction, whereas in the third and fourth columns it is along the x -direction, i.e., the direction along which the collision occurs. The first and the second rows show snapshots at $t = 2$ and 4 Myr of the “colliding” case. The bottom row corresponds to the $t = 4$ Myr snapshot for the “non-colliding” case.

istence of a double-peak in the p-v diagram. The corresponding velocity width has been estimated as $\sim 2 \text{ km s}^{-1}$. They explain this feature using smoothed particle hydrodynamics (SPH) simulations of two colliding cylinders (Duarte-Cabral et al. 2011) in which the resulting p-v diagram is reminiscent to the one observed in the Serpens region. Torii et al. (2011) provide p-v diagrams of the Trifid Nebula (M20) in which a broad bridge effect connecting multiple velocity peaks along the line-of-sight is observed. Similarly, Nakamura et al. (2012) presented high spatial resolution images of the $^{12}\text{CO } J = 1 - 0$ line for a wide region including the L1641-N cluster. They find two-velocity component gas along the line-of-sight suggesting a cloud-cloud collision event. The velocity width is $\sim 3 \text{ km s}^{-1}$ which is about three times higher than the local turbulent velocity ($v_{\text{turb}} \sim 1 \text{ km s}^{-1}$). Recently, Fukui et al. (2017a) identified double velocity peaks in the $^{12}\text{CO } J = 1 - 0$ line of the molecular gas toward M42 and M43, which potentially implies that the northern part of the Orion A cloud may have been formed by two colliding clouds.

Using hydrodynamical simulations, Haworth et al. (2015a,b) discuss extensively how the bridge effect occurs and develops in p-v diagrams of the $^{12}\text{CO } J = 1 - 0$ line. They examine various cases and at different viewing angles of colliding and non-colliding cases and they additionally examine p-v diagrams of isolated clouds. They also include modeling of radiative feedback (i.e., HII regions) generated by stars forming in their simulations. They find that the bridge feature holds for a small fraction of all possible viewing angles (e.g., about 20-30% for a $v_{\text{rel}} = 10 \text{ km s}^{-1}$ head-on collision, which is the collision velocity considered here) and is thus sensitive to the point of view of the observer. Furthermore, they find that this signature, when the geometry is favorable for its detection, is resilient to radiative feedback

from stars formed in the simulations and cannot be easily reproduced by kinematic behavior other than a cloud-cloud collision. A bridged double velocity peak can therefore act as a signature of an undergoing collision event.

Lines other than low- J CO (including isotopologues) have not been widely considered as diagnostic tracers for GMC-GMC collisions. However, Gerin et al. (2015) presented a detection of [CII] $158 \mu\text{m}$ at position G49.5-0.4 in W51A, in which strong emission from two velocity components is reported, i.e., $T_A \sim 30 \text{ K}$ and $\sim 25 \text{ K}$ for velocities of ~ 55 and $\sim 70 \text{ km s}^{-1}$, respectively. This implies a relative velocity of $v_{\text{rel}} \sim 15 \text{ km s}^{-1}$. W51A is considered to be a strong candidate of GMC-GMC collision activity (Ginsburg et al. 2015) and these observations, therefore, suggest that fine-structure lines may be possible diagnostic indicators for cloud collision events.

4. RESULTS

We construct integrated intensity emission maps and p-v diagrams for all three simulation snapshots considered (two for the colliding case at $t = 2$ and 4 Myr and one for the non-colliding case at $t = 4$ Myr). Our standard p-v diagrams are calculated by averaging over the entire y -direction at each different velocity, v , as a function of the z -direction. To highlight the bulk motions that are a signature of a cloud collision, we also show maps of integrated intensity of only higher velocities, i.e., $> +5 \text{ km s}^{-1}$ (redshifted) and $< -5 \text{ km s}^{-1}$ (blueshifted). This emission will mostly correspond to gas that moves at velocities greater than those reached due to internal turbulence. We focus our consideration on four different lines: $^{12}\text{CO } J = 1 - 0$ (hereafter CO $J = 1 - 0$); [C] ($609 \mu\text{m}$); [CII] $158 \mu\text{m}$; and [OI] $63 \mu\text{m}$.

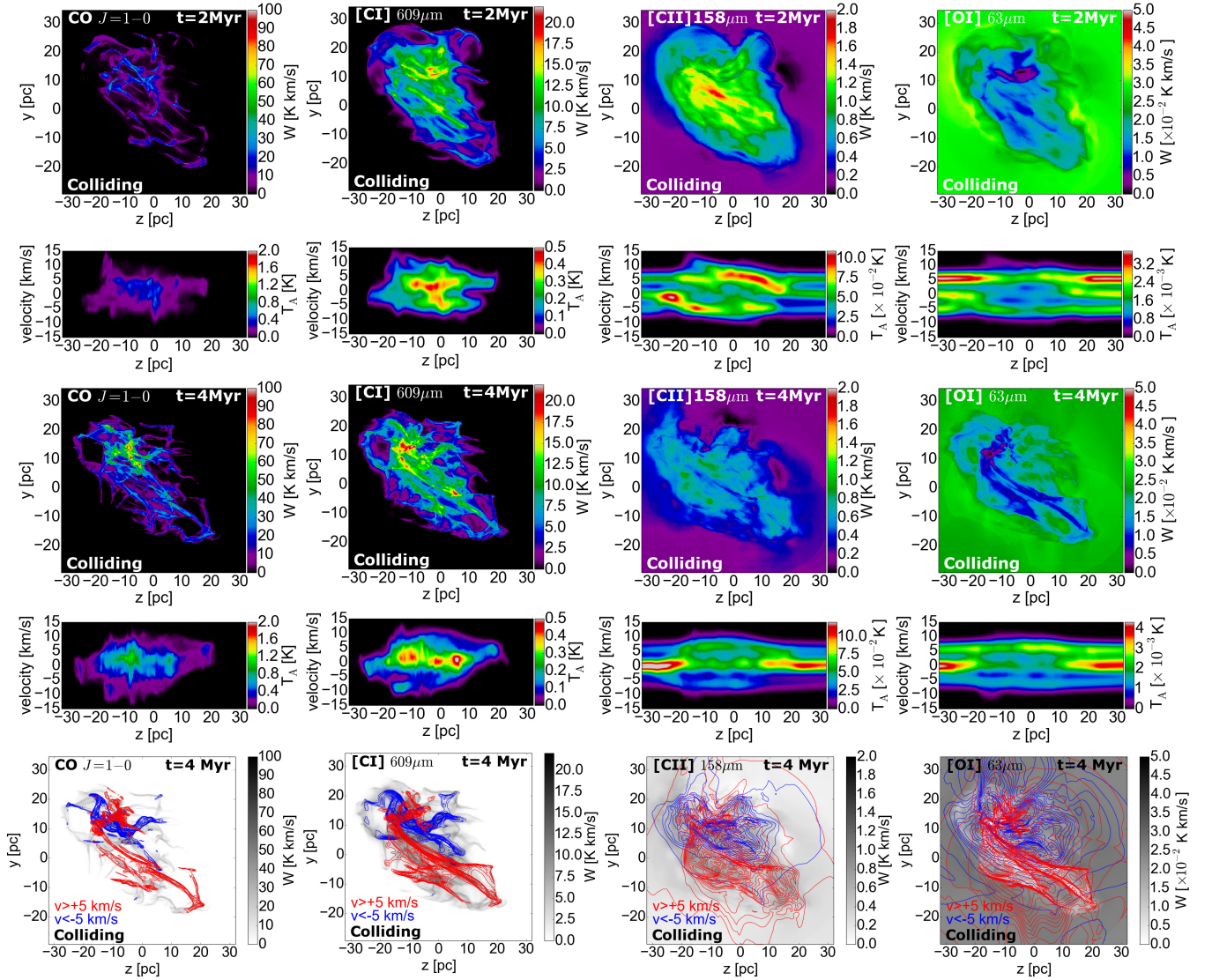


Figure 2. Emission maps (first and third rows) and position-velocity diagrams (second and fourth rows) for the colliding case at $t = 2$ Myr and 4 Myr, respectively. The collision occurs along the line-of-sight. Columns from left to right: CO $J = 1 - 0$; [CI] $609 \mu\text{m}$; [CII] $158 \mu\text{m}$; OI $63 \mu\text{m}$. The bottom row shows the integrated intensity of high velocity gas traced by each line at $t = 4$ Myr, i.e., maps the gas that has velocities $> +5 \text{ km s}^{-1}$ (red contours) and $< -5 \text{ km s}^{-1}$ (blue contours). The contours correspond to the intensity of the line. The grayscale shows the total intensity, W , of each line. In the p-v diagrams and at $t = 2$ Myr, the “bridge effect” is better seen in the fine-structure lines of [CII], [OI] and partially in the [CI] line, as all these are primarily emitted from the lower density gas, including from the ambient atomic medium, that has not yet undergone collision. Since CO $J = 1 - 0$ is emitted from the innermost part of both clouds where FUV radiation has been severely extinguished, identifying the collision signature in this line once the clouds start to merge is more difficult. Once the collision further evolves ($t = 4$ Myr), the bridge-effect is also diminished for the [CI] $609 \mu\text{m}$, although still holding in [CII] $158 \mu\text{m}$ and OI $63 \mu\text{m}$ lines. The maps of high velocity gas on the other hand show a collision event at $z \sim -10 \text{ pc}$ and $y \sim +10 \text{ pc}$ in CO $J = 1 - 0$ and [CI] $609 \mu\text{m}$, with the rest of the fine-structure lines indicating the bulk movement of GMCs and ambient medium on larger scales.

4.1. Colliding case

4.1.1. Fiducial results: comparison of CO and atomic fine structure lines

Figure 2 shows the emission maps (integrated intensity, W) and the corresponding p-v diagrams for the colliding case at $t = 2$ and 4 Myr for all different lines considered. The bottom row shows the high velocity gas emission for each case, which we discuss further below. These figures illustrate how each different species reveals different parts of the clouds and their surroundings.

The CO $J = 1 - 0$ transition, which has the strongest emission, originates from the densest parts of the GMCs. Since the collision occurs along the line-of-sight and the density increases as time progresses, at $t = 4$ Myr the intensity of this

CO transition is enhanced compared to that at 2 Myr. The enhancement is more prominent in the particular region located at $z \sim -10 \text{ pc}$ and $y \sim +10 \text{ pc}$, where the collision mainly occurs. Here, the total H-nucleus column density reaches a value of $\gtrsim 2 \times 10^{23} \text{ cm}^{-2}$. The enhancement in this line is partly because the higher density of the colliding region rapidly extinguishes the ambient FUV radiation field.

In the p-v diagrams, while the two velocity components of the original GMCs are just about discernible at 2 Myr, overall, and especially by 4 Myr, the emission becomes dominated by gas that has been compressed in the collision, i.e., near zero velocity in the simulation frame. Thus a bridge-effect signature linking two distinct peaks is not a characteristic feature of the CO $J = 1 - 0$ emission at these times.

We performed two additional investigations related to the

molecular gas emission. First, we examined the equivalent p - v diagrams of CO $J = 3 - 2$, which originates from relatively dense molecular gas. We found these p - v diagrams exhibit very similar morphologies to those of CO $J = 1 - 0$. Second, we constructed the p - v diagram of the CO $J = 1 - 0$ at $t = 1$ Myr, i.e., at an earlier stage of the evolution. We found that at this stage, the bridge-effect signature linking two distinct peaks was clearly visible, although its brightness temperature was much weaker than that shown in Fig. 2, since relatively fewer higher-density clumps were present at these earlier times.

The [C I] 609 μm line is primarily emitted from the more diffuse gas of both GMCs and hence it reveals the majority of the molecular gas of the clouds (see also Papadopoulos et al. 2004; Offner et al. 2014; Bisbas et al. 2015, 2017; Glover & Clark 2016). Note that its intensity remains approximately constant as time increases from $t = 2$ to $t = 4$ Myr.

The fine-structure line of [C II] 158 μm is emitted from the outer parts of both GMCs, since it is produced by the interaction with the isotropic FUV radiation field. This line is also emitted from the surrounding ambient medium, i.e., the ISM gas that is here set up as an idealized representation of atomic cold neutral medium with initial $n_{\text{H}} = 10 \text{ cm}^{-3}$, but also moving alongside each GMC and so forming a shock-compressed layer near zero velocity (see Paper II). The relative importance of the emission from the ambient medium compared to that from the GMCs is discussed below. In Fig. 2 we notice that the [C II] emission decreases in intensity from 2 to 4 Myr, which reflects the conversion of more material from the clouds in CO-emitting structures.

Similarly to [C II] 158 μm , the [O I] 63 μm line, although much weaker than all the above lines, originates from the outermost parts of both clouds and with significant contributions from the ambient medium. The 63 μm line is optically thick and due to this, its intensity is noticeably reduced at the parts of the map that correspond to high column densities (see Fig. 1). The blue-shifted component in the p - v diagrams (i.e., for $v_{\text{los}} \sim -5 \text{ km s}^{-1}$) has a reduced antenna temperature compared to the red-shifted component. The three well-defined stripes of antenna temperature correspond to the contribution of the ambient medium. The upper and lower stripes are due to the red-shifted and blue-shifted component respectively (moving away and towards the observer at a constant speed of $v_{\text{rel}} \pm 5 \text{ km s}^{-1}$). The central strip is mostly due to the shock compressed ambient medium (see §4.1.2). We further note that the [O I] line and in particular its ratio with [C I] 609 μm can be used as diagnostic of the intensity of the FUV radiation in PDRs (see Bisbas et al. 2014).

Summarizing the above results, the p - v diagrams in all cases span a width in velocity space $\sim \pm 10 \text{ km s}^{-1}$, i.e., resulting from the relative motion of both clouds, that is larger than that due to internal turbulence within the initial GMCs, i.e., $\sim \pm 5 \text{ km s}^{-1}$. Once the collision process begins, $W_{\text{CO}(1-0)}$ becomes enhanced. The motion of the gas then becomes more turbulent due to the collision as the two GMCs merge. This is reflected in the p - v diagram at $t = 4$ Myr in which the overall width in velocity space has increased. As a result, the double velocity peak feature that could indicate collision is diminished (see also Haworth et al. 2015b), although at the position $\sim -10 \text{ pc}$ (where the collision occurs) the intensity is quite strong over most of the velocity width of $\sim 20 \text{ km s}^{-1}$. The p - v diagram of the [C I] 609 μm line at $t = 2$ Myr indicates, however, that such a feature is reminiscent of the bridge-effect discussed in §3 and in particular

at position $\sim 0 \text{ pc}$. As time progresses and the clouds merge ($t = 4$ Myr), this signature disappears.

For systems whose collision is evolved to the point of erasing or diminishing any potential bridge-effect feature in the low- J CO p - v diagram, fine-structure lines may be promising alternatives to be diagnostics for such activity. This can be seen in the p - v diagrams of [C II] 158 μm and [O I] 63 μm ; these two lines give the most prominent signature of cloud-cloud collision, as the bridge effect linking two distinct peaks can now be clearly seen. However, as discussed above, the emission of both [C II] 158 μm and [O I] 63 μm lines originate mostly from the outer envelope of both GMCs and the surrounding ambient ISM gas, some of which corresponds to gas that has not yet suffered any collision and still carries the information of the relative velocity of GMCs prior to collision. They can thus be used in order to identify and/or clarify the collision process in systems whose low- J CO lines may provide limited information.

The bottom row of Fig. 2 shows the high velocity gas traced by each line. These maps correspond to the $t = 4$ Myr snapshots. The grayscale shows the total intensity, W , of each line. Red contours correspond to redshifted gas with velocities $v > +5 \text{ km s}^{-1}$ and blue contours to blueshifted gas with velocities $v < -5 \text{ km s}^{-1}$. In both cases, the contours correspond to the intensity of the line. We do not include velocities in the range $-5 < v < +5 \text{ km s}^{-1}$ as we want to isolate the bulk motion of the gas due to collision and the mutual interaction of the GMCs rather than additionally mapping the width reached due to turbulence. The Doppler shifts of both the CO $J = 1 - 0$ transition and the [C I] 609 μm line reveal the collision at $z \sim -10 \text{ pc}$ and $y \sim +10 \text{ pc}$ corresponding to the region with the highest density. However, the fine-structure line of [C II] 158 μm reveals the bulk movement of the GMCs and is thus a good indicator of the cloud-cloud collision.

4.1.2. Contribution of the ambient medium and the utility of the 158 μm line as a cloud-cloud collision diagnostic

Emission from the ambient, lower density medium can become important when studying the above fine-structure lines in these simulations. To clarify the contribution of this gas in our results, we calculate the p - v diagrams of [C II] 158 μm and [O I] 63 μm lines emitted by densities $n_{\text{H}} > 20 \text{ cm}^{-3}$ for the case at $t = 2$ Myr. For densities below 20 cm^{-3} , we consider negligible contribution in optical depth. This ensures that the p - v diagram will contain information that is essentially only from the GMCs. These results are shown in Fig. 3: the upper row shows the total emission and the bottom row shows the ‘‘GMC-only’’ emission. The bridge-effect is seen in the p - v diagram of [C II] 158 μm , as it is primarily emitted from the outer envelopes of the GMCs. Indeed, for our particular setup the GMC-only emission appears stronger since in the total case absorption from the ambient medium acts to diminish the signature of the collision. This may indicate an important role for $^{13}\text{C II}$ observations to complement [C II] studies (e.g. Goicoechea et al. 2015).

On the other hand, [O I] 63 μm is mainly emitted from the ambient medium and removing the contribution of the latter from our calculations results in a very weak brightness temperature (note that T_{A} in the bottom right panel of Fig. 3 is enhanced by a factor of 10). We thus find that the fine-structure line of [O I] 63 μm , being ambient medium dominated, is not, on its own, a good tracer of GMC-GMC collisions, but rather can give information on colliding atomic flows. However, since molecular clouds are known to have significant atomic

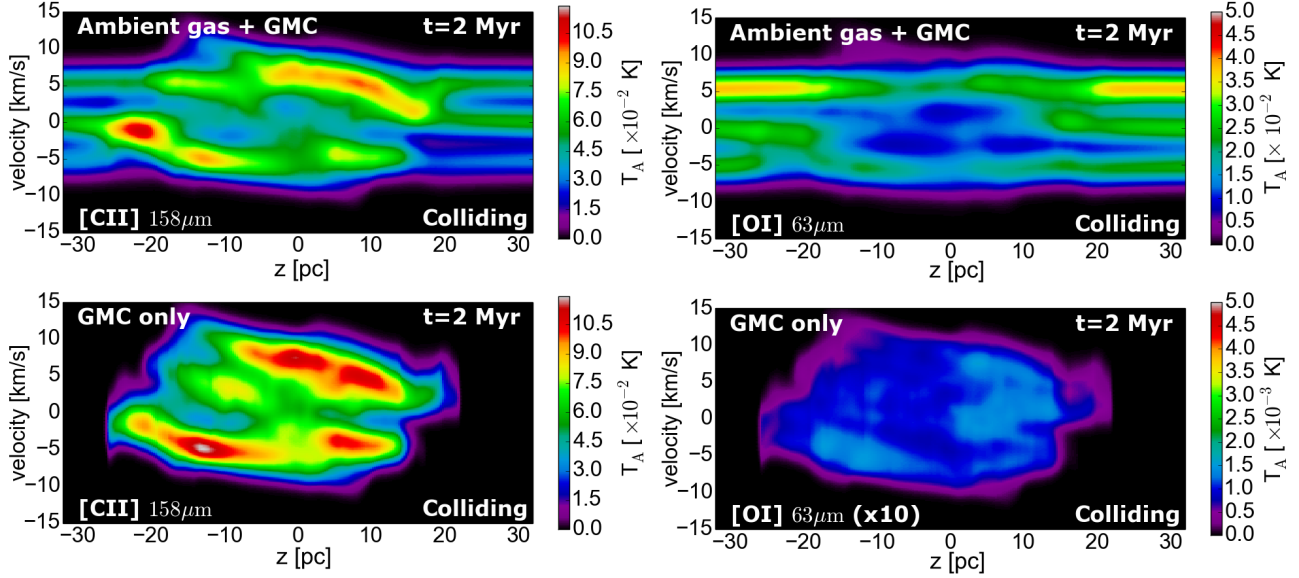


Figure 3. Position-velocity diagrams of [CII] $158\ \mu\text{m}$ (left column) and [OI] $63\ \mu\text{m}$ (right column) for the colliding case at $t = 2\ \text{Myr}$. In the top row, we include the contributions from both the ambient ISM and the GMC (i.e., same as in Fig. 2). In the bottom panel, we show only the contribution of the GMCs, i.e., selecting emission only from regions with $n_{\text{H}} > 20\ \text{cm}^{-3}$ (see §4.1.2). We find that [CII] $158\ \mu\text{m}$ emission is dominated by that from the GMCs, rather than the ambient medium. Indeed, the brightness temperature of the [CII] $158\ \mu\text{m}$ line emitted from the GMC-only case is stronger than the corresponding one from the total case, due to optical depth effects. However, the [OI] $63\ \mu\text{m}$ line emitted from the GMCs is significantly weaker than that from the ambient medium (note that we enhance the brightness temperature by a factor of 10 in the lower panel, to match the color-bar range of the upper panel). As such, the bridge-effect of GMC material is seen only in the [CII] line and not in [OI].

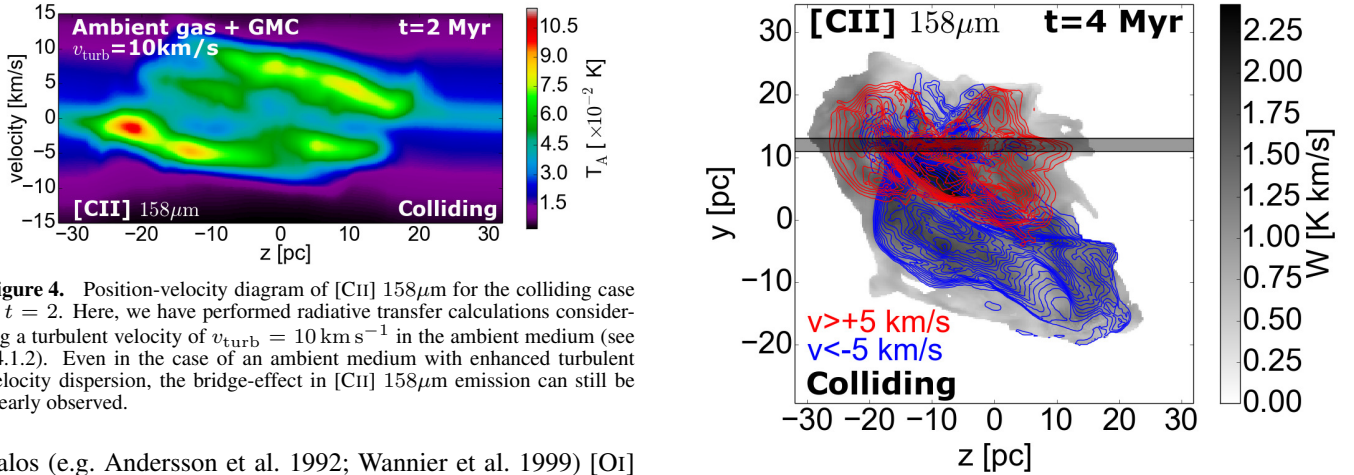


Figure 4. Position-velocity diagram of [CII] $158\ \mu\text{m}$ for the colliding case at $t = 2$. Here, we have performed radiative transfer calculations considering a turbulent velocity of $v_{\text{turb}} = 10\ \text{km s}^{-1}$ in the ambient medium (see §4.1.2). Even in the case of an ambient medium with enhanced turbulent velocity dispersion, the bridge-effect in [CII] $158\ \mu\text{m}$ emission can still be clearly observed.

halos (e.g. Andersson et al. 1992; Wannier et al. 1999) [OI] observations may still provide important complementary information for understanding particular collision candidates.

By design, the treatment of the ambient atomic medium in the Wu et al. (2017a) simulations is highly idealized. In particular, no internal turbulence is included in this component. Thus to explore potential effects of such turbulence, for the case of the [CII] $158\ \mu\text{m}$ line emission, we perform an additional radiative transfer calculation in which we assume an enhanced turbulent velocity (in post-processing) of $v_{\text{turb}} = 10\ \text{km s}^{-1}$ (see Eqn. A5) for densities below $20\ \text{cm}^{-3}$. Figure 4 shows the p-v diagram of this test. Comparing this with the corresponding figure in Fig. 2 (top left panel), we see that the velocity width is now increased and that the brightness temperature is moderately decreased. This is due to increased optical depth from the ambient medium over the range of velocities of [CII] emission from the GMCs. Still, we find that the bridge-effect is resilient to the uncertainties introduced from the emission of the ambient medium and the [CII] $158\ \mu\text{m}$ line is thus an important and useful diagnostic for GMC-GMC collisions.

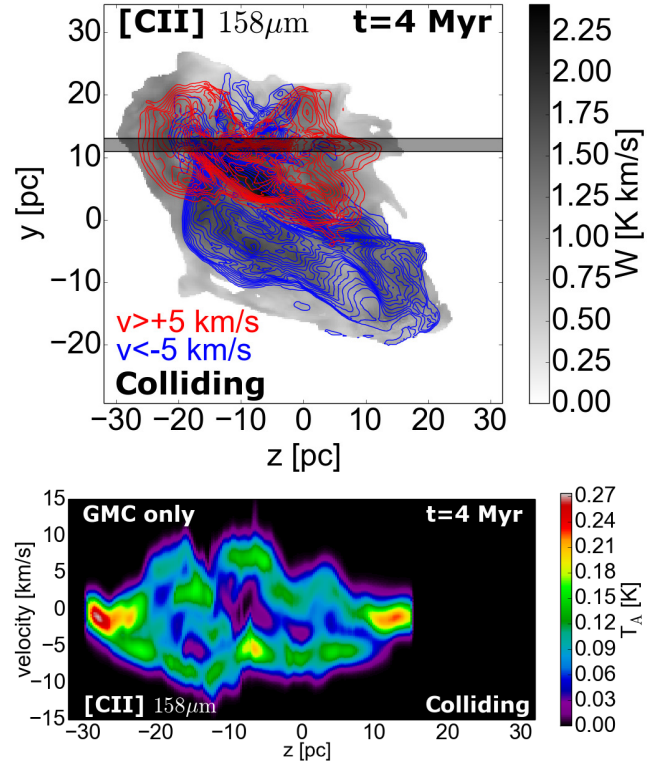


Figure 5. *Top panel:* High velocity gas in the [CII] $158\ \mu\text{m}$ line at $t = 4\ \text{Myr}$ when the contribution of the ISM has not been considered (GMC only case). It can be seen that the two red and blue shifted components overlap, indicating occurrence of a cloud collision. The shadowed strip of $2\ \text{pc}$ width, shows the part of the GMCs whose p-v diagram is shown in the bottom panel. *Bottom panel:* p-v diagram extracted from the 2-pc -wide strip through the dense overlap region. The high-velocity peaks in the upper panel are bridged indicating the collision is traced by the [CII] line.

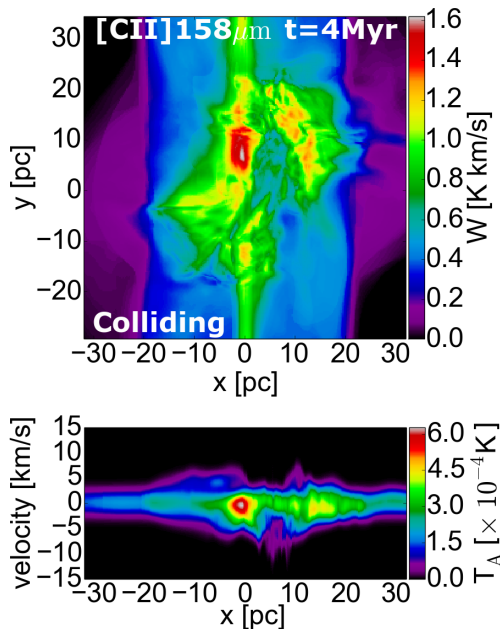


Figure 6. Emission map and p-v diagram of the colliding case in the [CII] $158\mu\text{m}$ line at $t = 4\text{ Myr}$. The radiative transfer calculations have been performed along the z -direction which is perpendicular to the direction of the collision. The stripe at $x \sim 0\text{ pc}$ and along the y -direction in the emission map is due to the collision of the ambient medium. As expected, in the p-v diagram we do not observe any feature pointing to a collision event. Instead, the width in velocity space is due to the internal gas motions (i.e., internal turbulence) rather than the bulk motion of each GMC.

The utility of [CII] $158\mu\text{m}$ as a diagnostic of cloud-cloud collisions is further demonstrated in Fig. 5, in which the upper panel shows a map of the high-velocity gas at $t = 4\text{ Myr}$ and where we exclude the contribution of the ambient medium. Extended parts of the high-velocity gas overlap, particularly in the region corresponding to the densest part of the colliding GMCs and where star formation is likely to be triggered (Paper III). We then isolate this part of emission map to construct a p-v diagram corresponding to a cut of only 2 pc width. This p-v diagram, also shown in Fig. 5, reveals that the emission peaks at distinct velocities are bridged in p-v space.

4.1.3. Effect of viewing angle - limiting case of a side-on view

In Fig. 6 we show the emission map and p-v diagram of the [CII] line at $t = 4\text{ Myr}$ when the observation is made perpendicular to the direction of the collision. In this case, any signature of the cloud-cloud collision is minimized, and the velocity width now is in principle connected with the internal turbulence of the gas. However, the emission map shows a characteristic feature of a rectangular shape spanning $\sim 40\text{ pc}$ (from -20 to $+20\text{ pc}$) with a bright stripe at $x \sim 0\text{ pc}$ across the y -axis. This originates from the ambient ISM gas in which both GMCs are embedded. The p-v diagram shows a single, main component in velocity space. Still, in the typical case one expects some part of the collision axis to be along the line of sight and the purely perpendicular case will be a relatively unlikely occurrence.

4.2. Non-colliding case

Figure 7 shows the emission maps, p-v diagrams and high velocity gas maps for the non-colliding case at $t = 4\text{ Myr}$. The emission maps in all four different lines are qualitatively similar to the colliding case at this dynamical time (see Fig. 2 for comparison). However, the intensities of CO $J = 1 - 0$

and [CI] $609\mu\text{m}$ are now lower since the system does not reach the necessary high densities and therefore the high column densities as in the colliding case. On the other hand, the emission maps of [CII] and [OI] lines do not significantly differ from the colliding case. The lower column densities reached in this simulation do not shield the $158\mu\text{m}$ line and it thus remains brighter than the corresponding one of Fig. 2.

The velocity widths of the p-v diagrams in Fig. 7 are all within the $-5 \lesssim v_{\text{los}} \lesssim +5\text{ km s}^{-1}$ range which results from the turbulent internal motion of the gas in both GMCs. An interesting feature, however, is that the intensity-weighted velocity gradients for the CO $J = 1 - 0$ and [CI] $609\mu\text{m}$ lines are decreasing along the position axis in the p-v diagrams. This is due to the mutual gravitational forces attracting the GMCs towards each other in the simulation domain. These gradients are most clearly seen in the high velocity gas maps in the bottom row of the figure. Here it can be seen that the red- ($v_{\text{los}} > +5\text{ km s}^{-1}$) and blue- ($v_{\text{los}} < -5\text{ km s}^{-1}$) shifted components do not overlap as shown in the bottom row of Fig. 2, different from the cloud-cloud collision case. For example, for the particular geometries considered we find a $\lesssim 17\%$ overlap in the [CII] $158\mu\text{m}$ line as opposing to a $\gtrsim 42\%$ in the colliding case (when compared to the upper panel of Fig. 5).

5. DISCUSSION

Being able to identify collisions between GMCs is potentially important for our understanding of the global star formation process in galaxies. As discussed in §3, observational surveys have revealed several cases of on-going cloud-cloud collisions using low- J CO lines as diagnostics. Our work complements these findings by first analyzing the results of realistic MHD simulations of colliding, turbulent, multiphase GMCs, and then exploring how fine-structure lines compare with CO $J = 1 - 0$. This work differs from the studies of Haworth et al. (2015a,b) by considering a more realistic physical model that includes magnetic fields and PDR-based heating/cooling, a concomitant improved treatment for the abundance and level populations of CO (whereas they assumed a constant abundance of $[\text{CO}]/[\text{H}] = 8 \times 10^{-5}$ throughout their clouds), and a calculation of the radiative transfer of the fine-structure lines.

Our main finding is that the lines of [CI] $609\mu\text{m}$ and [CII] $158\mu\text{m}$, are promising alternative ways for identifying cloud-cloud collisions via the bridge-effect, linking distinct velocity peaks in p-v space. The [OI] $63\mu\text{m}$ line is highly affected by the contribution of the ambient ISM, so its emission will depend sensitively to the nature of the atomic gas around the GMCs. Such gas has only been treated in a very idealized way in our current simulations, so we are not able to draw strong conclusions about the utility of [OI] as a GMC-GMC collision diagnostic, however, we expect it may be potentially useful if GMCs have significant co-moving atomic halos. As the collision progresses and the denser parts of the clouds merge, the bridge-effect diminishes and low- J CO lines then hardly show any signature of the collision. On the other hand, the lifetime of the broad bridge in fine-structure lines is predicted to be longer since these lines are emitted from the more rarefied parts of GMCs which are primarily located at their outer envelopes that have not yet undergone collision.

The models considered here are based on an idealized situation in which there is no local stellar feedback. However, cloud-cloud collisions are potential sites for triggered star formation (Fukui et al. 2015, 2017a,b; Torii et al. 2015, 2017a),

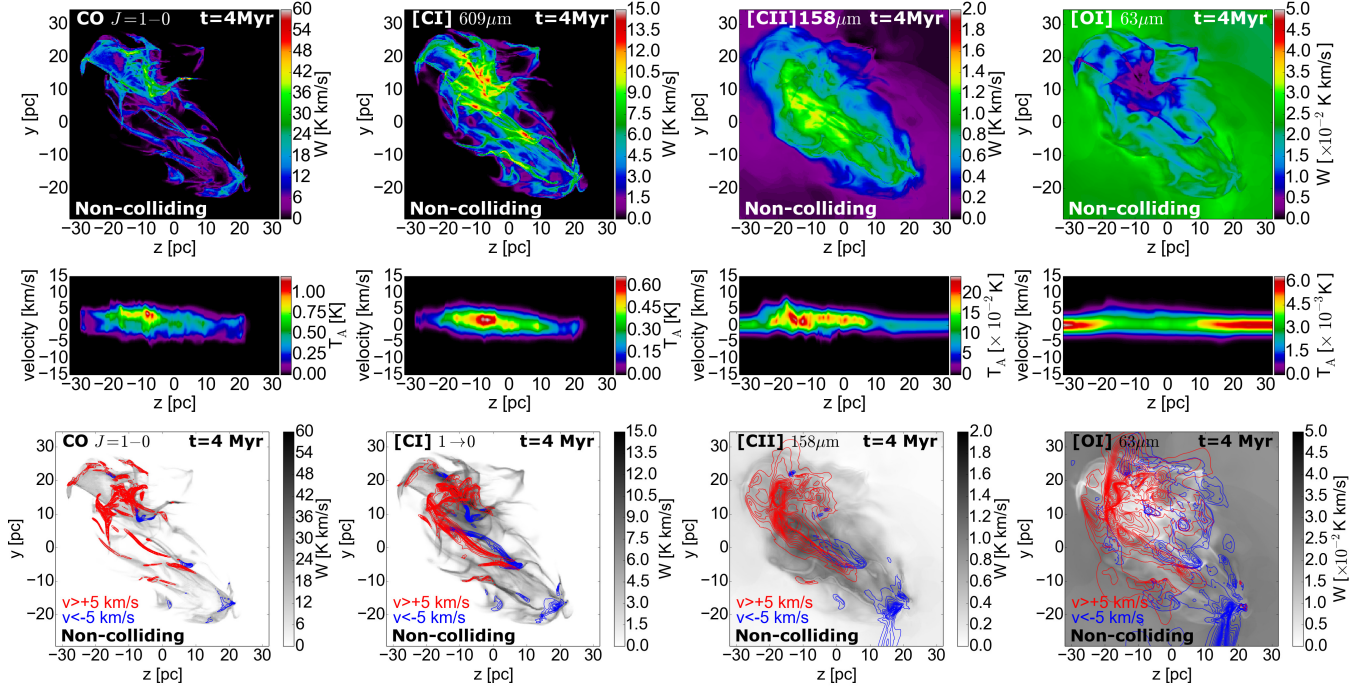


Figure 7. As in Fig. 2, but now for the non-colliding case. Here we plot the emission maps, p-v diagrams and the high velocity gas for $t = 4$ Myr only. From the p-v diagrams it can be seen that in all cases we find a width of $< 8 \text{ km s}^{-1}$ corresponding to the turbulent velocity dispersion due to the internal gas motions in each GMC. However, the gravitational forces acting on both clouds result in their mutual attraction. This can be observed in the high velocity gas maps in which the upper-left part is redshifted and the bottom-right is blueshifted. Still, in none of the cases do we observe an interaction pointing to a collision, such as seen in Fig. 2.

including leading to the birth of massive, $> 10 M_{\odot}$ stars (Takahira et al. 2014; Balfour et al. 2015). Thus the signatures of the PDRs from such localized stellar feedback (see, e.g., for examples of models of HII region feedback Dale et al. 2012; Walch et al. 2015; Haworth et al. 2015a) may confuse those from the bulk original GMC material, externally irradiated. Such contributions also need to be accounted for when interpreting observational data that includes localized PDRs, although recent simulations by Torii et al. (2017b) indicate that feedback of such massive stars does not alter the bridge-effect in p-v diagrams of molecular lines, such as low- J ^{12}CO . Thus the models presented here are most useful for isolating the “pure” signature of the GMC-GMC collision, which may be most easily compared to observations of GMCs in relatively early stages of collision and star formation.

Another simplification of our treatment is that in the post-processing of the MHD simulations, the gas is assumed to be in local thermodynamic equilibrium and additional transient heating effects from shocks are ignored. A future paper in this series will explore the importance of such effects.

As discussed in §4, most of our presented results are for the case of the collision occurring along the line-of-sight of the observer, which is the most idealized situation. In general, the detectability of the bridge-effect signature will diminish as the fraction of the collision axis that is projected along the line of sight decreases. To overcome such effects, statistically significant samples of GMC-GMC collision candidates need to be considered.

6. CONCLUSIONS

In this paper we performed synthetic observations of ^{12}CO $J = 1 - 0$, [CI] $609 \mu\text{m}$, [CII] $158 \mu\text{m}$ and [OI] $63 \mu\text{m}$ based on snapshots of MHD simulations of GMC collisions, carried out in Paper II of this series. The selected snapshots examine

the colliding case of two GMCs, and the non-colliding case of two GMCs that overlap each other along the line-of-sight of the observer. With a simple radiative transfer tool, we calculated integrated intensity emission maps (including of high velocity components) and position-velocity diagrams for the above lines. We demonstrated that fine-structure lines, and in particular [CII] $158 \mu\text{m}$, may be a promising alternative diagnostic of cloud-cloud collisions, separate from the more commonly discussed CO lines. This finding holds even when the collision has been evolved so that the denser regions have merged and that low- J CO lines are no longer good tracers of the collision. Our results are summarized as follows:

- The overall CO $J = 1 - 0$ emission is stronger in the colliding than in the non-colliding case and in particular at the region where the collision occurs (peak of the total H-nucleus column density). The p-v diagram in the colliding case does not show a clear signature of the bridge-effect, mainly because the collision has been evolved to an extent that the CO-rich gas has been mixed up and such a signature is diminished. On the other hand, the integrated intensity maps of blue- and redshifted high velocity gas do show in a clear way whether or not the two GMCs along the line-of-sight are colliding.
- The [CI] $^3\text{P}_1 \rightarrow ^3\text{P}_0$ transition corresponding to a wavelength of $609 \mu\text{m}$ is found to be emitted from the more diffuse gas of both GMCs. Although it peaks at the position where the two GMCs collide, it does not fluctuate as much as the CO $J = 1 - 0$ line and its intensity does not significantly differ in the non-colliding case. The bridge-effect is observable in the p-v diagram at $t = 2$ Myr in the colliding case, however at $t = 4$ Myr it has disappeared. As with the CO $J = 1 - 0$

line, the high velocity maps are able to indicate the collision event at all times.

- The fine-structure [CII] $158\ \mu\text{m}$ shows the clearest signature of the bridge-effect in the p-v diagrams of the colliding case. This line is emitted from the outermost parts of both GMCs, with modest further contributions from the ambient ISM gas. We find that the contribution of the ambient ISM does not significantly impact the ability of [CII] $158\ \mu\text{m}$ to be a tracer of GMC-GMC collisions. The overall [CII] emission does decrease in time as the collision progresses, since the increase in density shields the FUV radiation. The blue- and redshifted high velocity gas overlap almost everywhere in the colliding case.
- The emission of the [OI] $^3\text{P}_1 \rightarrow ^3\text{P}_0$ transition at $63\ \mu\text{m}$ is much weaker than that of [CII] at $158\ \mu\text{m}$, with significant contributions from the ambient atomic ISM gas. It is thus a better tracer of surrounding atomic halos of GMCs, which, depending on their properties, may provide important, complementary information to diagnose GMC-GMC collisions.

All p-v diagrams in the non-colliding case show a velocity width corresponding to internal turbulent gas motions, i.e., at approximately virialized velocities. Furthermore, in all the above cases, we have assumed that the collision occurs along the line-of-sight of the observer. If the collision is viewed at an angle, then any potential signatures will be diminished and completely eliminated in the cases that the collision occurs mostly perpendicular to the observer. Statistical samples of GMC-GMC collision candidate events are needed to average over such geometric effects.

The authors thank an anonymous referee whose comments improved the clarity of the paper. We thank Thomas Haworth, Adam Ginsburg and Guang-Xing Li for useful discussions. KT thanks Kazuhito Motogi, Taishi Nakamoto and Hideko Nomura. BW is thankful for support from the Japan Society for the Promotion of Science Postdoctoral Fellowship.

REFERENCES

Andersson, B.-G., Wannier, P. G., & Lewis, B. M. 1992, *MNRAS*, 254, 7
 Andree-Labsch, S., Ossenkopf-Okada, V., & Röllig, M. 2017, *A&A*, 598, A2
 Balfour, S. K., Whitworth, A. P., Hubber, D. A., & Jaffa, S. E. 2015, *MNRAS*, 453, 2471
 Bisbas, T. G., Bell, T. A., Viti, S., Yates, J., & Barlow, M. J. 2012, *MNRAS*, 427, 2100
 Bisbas, T. G., Bell, T. A., Viti, S., et al. 2014, *MNRAS*, 443, 111

Bisbas, T. G., Papadopoulos, P. P., & Viti, S. 2015, *ApJ*, 803, 37
 Bisbas, T. G., van Dishoeck, E. F., Papadopoulos, P. P., et al. 2017, *ApJ*, 839, 90
 Bryan, G. L., Norman, M. L., O’Shea, B. W., et al. 2014, *ApJS*, 211, 19
 Cardelli, J. A., Meyer, D. M., Jura, M., & Savage, B. D. 1996, *ApJ*, 467, 334
 Cartledge, S. I. B., Lauroesch, J. T., Meyer, D. M., & Sofia, U. J. 2004, *ApJ*, 613, 1037
 Christie, D., Wu, B., & Tan, J. C. 2017, arXiv:1706.07032
 Dale, J. E., Ercolano, B., & Bonnell, I. A. 2012, *MNRAS*, 424, 377
 Dobbs, C. L., Pringle, J. E., & Duarte-Cabral, A. 2015, *MNRAS*, 446, 3608
 Draine, B. T. 2011, *Physics of the Interstellar and Intergalactic Medium* by Bruce T. Draine. Princeton University Press, 2011. ISBN: 978-0-691-12214-4,
 Duarte-Cabral, A., Fuller, G. A., Peretto, N., et al. 2010, *A&A*, 519, A27
 Duarte-Cabral, A., Dobbs, C. L., Peretto, N., & Fuller, G. A. 2011, *A&A*, 528, A50
 Fukui, Y., Torii, K., Hattori, Y., et al. 2017a, arXiv:1701.04669
 Fukui, Y., Tsuge, K., Sano, H., et al. 2017b, *PASJ*, 69, L5
 Fukui, Y., Harada, R., Tokuda, K., et al. 2015, *ApJ*, 807, L4
 Fukui, Y., Ohama, A., Hanaoka, N., et al. 2014, *ApJ*, 780, 36
 Gammie, C. F., Ostriker, J. P., & Jog, C. J. 1991, *ApJ*, 378, 565
 Gerin, M., Ruaud, M., Goicoechea, J. R., et al. 2015, *A&A*, 573, A30
 Ginsburg, A., Bally, J., Battersby, C., et al. 2015, *A&A*, 573, A106
 Glover, S. C. O., & Clark, P. C. 2016, *MNRAS*, 456, 3596
 Goicoechea, J. R., Teyssier, D., Etzaluz, M., et al. 2015, *ApJ*, 812, 75
 Habing, H. J. 1968, *Bull. Astron. Inst. Netherlands*, 19, 421
 Haworth, T. J., Tasker, E. J., Fukui, Y., et al. 2015a, *MNRAS*, 450, 10
 Haworth, T. J., Shima, K., Tasker, E. J., et al. 2015b, *MNRAS*, 454, 1634
 Higuchi, A. E., Kurono, Y., Saito, M., & Kawabe, R. 2010, *ApJ*, 719, 1813
 Inoue, T., & Fukui, Y. 2013, *ApJ*, 774, L31
 Jin, K., Salim, D. M., Federrath, C., et al. 2017, *MNRAS*, 469, 383
 Li, Q., Tan, J. C., Christie, D., Bisbas, T. G., & Wu, B. 2017, arXiv:1706.03764
 McElroy, D., Walsh, C., Markwick, A. J., et al. 2013, *A&A*, 550, A36
 Nakamura, F., Miura, T., Kitamura, Y., et al. 2012, *ApJ*, 746, 25
 Offner, S. S. R., Bisbas, T. G., Bell, T. A., & Viti, S. 2014, *MNRAS*, 440, L81
 Papadopoulos, P. P., Thi, W.-F., & Viti, S. 2004, *MNRAS*, 351, 147
 Röllig, M., Abel, N. P., Bell, T., et al. 2007, *A&A*, 467, 187
 Scoville, N. Z., Sanders, D. B., & Clemens, D. P. 1986, *ApJ*, 310, L77
 Suwannajak, C., Tan, J. C., & Leroy, A. K. 2014, *ApJ*, 787, 68
 Takahira, K., Tasker, E. J., & Habe, A. 2014, *ApJ*, 792, 63
 Tan, J. C. 2000, *ApJ*, 536, 173
 Tan, J. C. 2010, *ApJ*, 710, L88
 Tan, J. C., Shaske, S. N., & Van Loo, S. 2013, *Molecular Gas, Dust, and Star Formation in Galaxies*, 292, 19
 Tasker, E. J., & Tan, J. C. 2009, *ApJ*, 700, 358
 Torii, K., Hattori, Y., Matsuo, M., et al. 2017b, arXiv:1706.07164
 Torii, K., Hattori, Y., Hasegawa, K., et al. 2017a, *ApJ*, 835, 142
 Torii, K., Hasegawa, K., Hattori, Y., et al. 2015, *ApJ*, 806, 7
 Torii, K., Enokiy, R., Sano, H., et al. 2011, *ApJ*, 738, 46
 Walch, S., Whitworth, A. P., Bisbas, T. G., Hubber, D. A., & Wünsch, R. 2015, *MNRAS*, 452, 2794
 Wannier, P., Andersson, B.-G., Penprase, B. E., & Federman, S. R. 1999, *ApJ*, 510, 291
 Wu, B., Van Loo, S., Tan, J. C., & Bruderer, S. 2015, *ApJ*, 811, 56
 Wu, B., Tan, J. C., Nakamura, F., et al. 2017a, *ApJ*, 835, 137
 Wu, B., Tan, J. C., Christie, D., et al. 2017b, *ApJ*, 841, 88

APPENDIX

RADIATIVE TRANSFER ALGORITHM

We describe here the algorithm of radiative transfer calculations we develop which was used in all synthetic maps in this work (see also §2.3). We begin by solving the radiative transfer equation along the line-of-sight element dz :

$$\frac{dI_\nu}{dz} = -\alpha_\nu I_\nu + \alpha_\nu S_\nu, \quad (\text{A1})$$

where I_ν is the intensity of the line, α_ν the absorption coefficient, and S_ν is the source function at frequency ν . The source function and the absorption coefficient for a transition of $i \rightarrow j$ are

$$S_\nu = \frac{2h\nu_0^3}{c^2} \frac{n_i g_j}{n_j g_i - n_i g_j}, \quad (\text{A2})$$

$$\alpha_\nu = \frac{c^2 n_i A_{ij}}{8\pi\nu_0^2} \left(\frac{n_j g_i}{n_i g_j} - 1 \right) \phi_\nu, \quad (\text{A3})$$

where ν_0 is the frequency of the line center, A_{ij} is the Einstein A coefficient, n_i, n_j are the level populations, and g_u, g_l are the statistical weights of levels i, j , and ϕ_ν is the line profile. The level populations are obtained from our photodissociation region calculations using 3D-PDR (see §2.2 Bisbas et al. 2012). We assumed a Maxwellian distribution of velocities due to the thermal and the turbulent gas motion. The line profile takes, therefore, the form

$$\phi_\nu = \frac{1}{\sqrt{2\pi\sigma_\nu^2}} \exp \left\{ -\frac{[(1 + v_{\text{los}}/c)\nu - \nu_0]^2}{2\sigma_\nu^2} \right\}, \quad (\text{A4})$$

where v_{los} is the gas velocity along the line-of-sight (positive for red-shift and negative for blue-shift), and σ_ν is the dispersion defined as

$$\sigma_\nu = \frac{\nu_0}{c} \sqrt{\frac{k_B T_{\text{gas}}}{m_{\text{mol}}} + \frac{v_{\text{turb}}^2}{2}}, \quad (\text{A5})$$

where T_{gas} is the gas temperature, m_{mol} is the mass of the molecule/ion emitting the line, and v_{turb} is the a root mean-square measure of turbulent velocities (set to be $v_{\text{turb}} = 1.5 \text{ km s}^{-1}$ throughout the radiative transfer calculations presented here).

The formal solution of radiative transfer equation (Eqn. A1) is given by

$$I_\nu(z) = I_\nu(0)e^{\tau_\nu(z)} + \int_0^{\tau_\nu(z)} S_\nu(z')e^{\tau'_\nu - \tau_\nu(z)} d\tau'_\nu, \quad (\text{A6})$$

where $\tau_\nu = \int_0^z \alpha_\nu(z')dz'$ is the optical depth. To solve the radiative transfer numerically, the absorption coefficient is assumed to be a linear function of z and the source function is assumed to be a linear function of τ between each grid $[z_p, z_{p+1}]$ (see also Andree-Labsch et al. 2017, for alternative ways of solving the radiative transfer equation in this limit). Then, the differential solution can be obtained as

$$I_{\nu,p+1} = I_{\nu,p}e^{-\Delta\tau_\nu} + S_{\nu,p} \left(\frac{1 - e^{-\Delta\tau_\nu}}{\Delta\tau_\nu} - e^{\Delta\tau_\nu} \right) + S_{\nu,p+1} \left(1 - \frac{1 - e^{-\Delta\tau_\nu}}{\Delta\tau_\nu} \right), \quad (\text{A7})$$

$$\Delta\tau_\nu = \frac{\alpha_{\nu,p} + \alpha_{\nu,p+1}}{2} dz, \quad (\text{A8})$$

where the subscripts of p and $p + 1$ denote the position of variables. This form of the solution can reproduce the physical consequences at both optically thin and thick limits:

$$I_{\nu,p+1} = \begin{cases} I_{\nu,p}(1 - \Delta\tau_\nu) + \frac{B_{\nu,p} + B_{\nu,p+1}}{2} \Delta\tau_\nu & (\Delta\tau_\nu \rightarrow 0), \\ B_{\nu,p+1} & (\Delta\tau_\nu \rightarrow \infty). \end{cases} \quad (\text{A9})$$

For boundary conditions, we adopt the intensity of the Cosmic Microwave Background Radiation of 2.7 K, i.e. $I_\nu(z = 0) = B_\nu(2.7K)$ where B_ν is the Planck function. The line profile is obtained by solving Eqn. A6 for the frequency range $[\nu_0 - \Delta\nu/2, \nu_0 + \Delta\nu/2]$, where $\Delta\nu \ll \nu_0$ is the band width.